Contents list available at the CBIORE journal website

International Journal of Renewable Energy Development

Journal homepage: https://ijred.cbiore.id

Research Article

Comparative study of g-C_3N_4/Cu_2O and $BiVO_4$/Cu_2O photocathodes for enhanced electricity generation and hydrogen evolution in photocatalytic fuel cells

Muhammad Fahmi Hakim[a,b], Muhammad Febriansyah Bachri[a], Ratnawati[c], Rike Yudianti[d], Muhammad Ibadurrohman[a], Slamet[a*]

[a]*Department of Chemical Engineering, Faculty of Engineering, Universitas Indonesia, Depok 16424, Indonesia*

[b]*Department of Chemical Engineering, Faculty of Engineering, Universitas Singaperbanga Karawang, Karawang 41361, Indonesia*

[c]*Department of Chemical Engineering, Institut Teknologi Indonesia, Tangerang Selatan 15314, Indonesia*

[d]*Research Center for Nanotechnology System, National Research and Innovation Agency (BRIN), South Tangerang 15314, Indonesia*

Abstract. The preparation of good photocathodes is a crucial issue regarding promoting the performance of photocatalytic fuel cell (PFC) systems for environmentally protective energy conversion approaches. In the present work, a comparative study of Cu_2O-based photocathodes jointly modified with graphitic carbon nitride (g-C_3N_4) and bismuth vanadate ($BiVO_4$) was performed to ascertain their competence towards concomitant electricity generation and hydrogen evolution in an integrated single-chamber photocatalytic fuel cell. Cu substrates were anodized to produce ordered Cu_2O layers, modified with immersion treatments, and then low-temperature calcination. The as-prepared products were characterized in detail by XRD, HR-TEM, UV–Vis DRS, PL spectra, and XPS analyses, as well as photoelectrochemical measurements to gain insight into crystallinity, morphology, photocatalytic activity (optical absorption), electronic structure, and charge recombination. Results revealed that among the pristine Cu_2O and g-C_3N_4/Cu_2O, superior charge separation was exhibited on the $BiVO_4$/Cu_2O photocathode, along with better power density and hydrogen evolution. The highest power density of $BiVO_4$/Cu_2O was 0.05625 mW cm^{-2} and 13.71 mmol.m^{-2} for hydrogen evolution compared to both Cu_2O (0.0375 mW cm^{-2};11.19 mmol.m^{-2}) and g-C_3N_4/Cu_2O (0.026 mW cm^{-2}; 8.1616 mmol m^{-2}). This observation was supported by the analysis of the photoluminescence spectra: $BiVO_4$/Cu_2O had PL intensity of 325 a.u., lower than Cu_2O (400 a.u.) and g-C_3N_4/Cu_2O (650 a.u.), validating that this sample more effectively suppressed electron–hole recombination and electron transport mechanism. The enhanced photocatalytic activity of $BiVO_4$/Cu_2O is associated with the generation of a p-n heterojunction, which accumulates a built-in electric field to drive effective charge separation and offers visible-light sensitization upon its larger absorption spectrum that is beneficial for not only promoting hydrogen evolution efficiency but also improving electricity production in PFC systems.

Keywords: Cu_2O, photocathode, hydrogen evolution, photocatalytic fuel cell, Z-scheme.

Received: 22nd Sept 2025; Revised: 18th Nov 2025; Accepted: 23rd Dec 2025; Available online: 30th Dec 2025.

1. Introduction

The growing demand for renewable energy and stricter environmental regulations has increased the need for clean and decentralized energy systems. Hydrogen has garnered a lot of interest as a possible fuel for the energy infrastructure of the future because to its carbon-free qualities, high energy density, and portability among green energy carriers. One intriguing solar-driven device that can generate both power and hydrogen at the same time is the photocatalytic fuel cell (PFC). (Liu *et al.*, 2024; Rehan *et al.*, 2025). The photoelectrode, and the photocathode in particular, are crucial to the operation of PFCs since they are the ones that really carry out the hydrogen evolution process (HER). (He *et al.*, 2019). Cu_2O, or copper(I) oxide, is a fascinating material for use as a photocathode since it is a p-type semiconductor with a suitable bandgap (~2.2 eV) and an advantageous conduction band edge for HER. (Hamdani & Bhaskarwar, 2021) (N. Li *et al.*, 2024). However, Cu_2O photocatalytic efficacy is severely limited due to its electron-hole recombination and weak photostability. Surface modification and semiconductor coupling, two methods of heterojunction engineering, have been extensively investigated as potential solutions to these limitations (Lu *et al.*, 2025).

The 2D polymeric semiconductor graphitic carbon nitride (g-C_3N_4) has a bandgap of 2.7 eV, excellent visible light absorption capabilities, and excellent thermal and chemical durability. The formation of a p-n heterojunction by g-C_3N_4 complexed with Cu_2O has many benefits, including enhanced photocatalytic activity, longer lifespan, photoelectron-hole recombination, and charge separation and adsorption (Mamari *et al.*, 2021; Dai *et al.*, 2022).

Conversely, in the type-II or Z-scheme structure, the n-type semiconductor bismuth vanadate ($BiVO_4$) serves as an effective electron mediator due to its visible area and about 2.4 eV band gap. Incorporating $BiVO_4$ enhances the photocathode

* Corresponding author
Email: slamet@che.ui.ac.id (S. Slamet)

https://doi.org/10.61435/ijred.2026.61810
ISSN: 2252-4940/© 2026.The Author(s). Published by CBIORE

surface's reduction capacity, stability, and photocurrent production capabilities. (Dai *et al*., 2022; Lin *et al*., 2014; Cheng *et al*., 2025).

Their heterojunction systems have been extensively researched, but their use as photocathodes for PFCs, particularly for the evolution of both hydrogen and electricity at the same time, has been reported only seldom. Therefore, according (Sienkiewicz *et al*., 2021). a mix of anodization and immersion-calcination methods was used to create Cu_2O photocathodes modified with g-C_3N_4 or $BiVO_4$. A single-chamber PFC was used to test the electrodes, and the electrolyte was made from POME, which is a byproduct of the palm oil mill. A thorough assessment using structural, optical, and photoelectrochemical studies showed how each alteration affected charge transfer, photostability, and overall photocathodic performance.

The novelty of this study lies in two key aspects. First, this work employs a flat Cu metal plate as the conductive substrate, which is directly converted into Cu_2O and further modified into g-C_3N_4/Cu_2O and $BiVO_4$/Cu_2O heterojunctions. This approach provides shorter electron pathways, stronger interfacial bonding, and improved mechanical stability compared with conventional FTO, ITO, carbon cloth, or Cu foam-based photocathodes. Second, both heterojunction photocathodes are integrated into a single-chamber PFC combining hydrogen evolution and electricity generation, enabling one of the first systematic evaluations of two distinct Cu_2O heterostructures within the same operating configuration.

2. Materials and Methods

2.1 Materials and Reagents

There were no further purifying procedures performed on any of the compounds used in this investigation; they were all of the pro-analysis grade. The photocathode was manufactured using a purified copper (Cu) plate with a thickness of 0.3 mm and a purity of 99.9% or higher. We got ammonium metavanadate (NH_4VO_3), bismuth pentahydrate nitrate ($Bi(NO_3)_3{\cdot}5H_2O$), melamine, and potassium hydroxide (KOH) from Merck. During synthesis, ethanol and deionized water were used for all cleaning and dissolving operations.

2.2 Synthesis of Cu_2O-based Photocathodes

Two sorts of photocathodes, g-C_3N_4/Cu_2O and $BiVO_4$/Cu_2O, were fabricated respectively. The Cu substrates were transformed to Cu_2O by anodization and surface modified using immersion and calcination methods, respectively.

2.2.1 Formation of Cu_2O Layer via Anodization

After being ultrasonically cleaned in 0.25 M HCl, acetone, ethanol, and deionized water in sequence, the 8x4 cm copper plates were dried. In a 2 M KOH solution, electrolyte anodization was carried out for 20 minutes at room temperature with a voltage of 1.2 V (Bachri *et al*., 2025).

2.2.2 Modification with g-C_3N_4

Graphitic “carbon nitride” (g-C_3N_4) was prepared thermally by the heating of melamine powder in a closed crucible at 550 °C for 2 hours in a furnace, and it appeared as a yellow powder (Husein *et al*., 2024). For the preparation of g-C_3N_4/Cu_2O composite, the anodized Cu_2O was ultrasonicated in the g-C_3N_4 suspension, which was synthesized by ultrasonication of 0.5 g g-C_3N_4 in isopropyl alcohol for 5 min and then was left to stand for 15 h. The samples were sintered at 350 °C for 1 hour under nitrogen with a heating rate of 5 °C min^{-1}.

2.2.3 Modification with $BiVO_4$

The $BiVO_4$/Cu_2O composite was made by burning the anodized Cu_2O plates for one hour at 350°C in a nitrogen environment at a rate of 5°C/min. The $BiVO_4$ precursor solution was prepared as follows: First, 100 mL of deionized water was used to dissolve 0.485 g of $Bi(NO_3)_3.5H_2O$ (Solution A). Then, 100 mL of hot deionized water at 70 °C was used to dissolve 0.117 g of NH_4VO_3 (Solution B). Ten minutes were spent stirring the two liquids together. Then, the Cu_2O electrodes were immersed in the mixture for 3 h (optimized duration). These conditions were selected based on preliminary trials to ensure uniform coating, good interfacial contact, and phase stability of both Cu_2O and the deposited layer without inducing over-oxidation or structural degradation.. the Cu_2O electrodes were removed and allowed to dry naturally. The last step was to calcine the electrode in air at 200 °C for an hour.

2.3 Characterization Techniques

The crystalline phase and the microstructure of the samples were identified using X-ray diffraction (XRD, PANalytical X'Pert PRO, Cu Kα radiation), transmission electron microscopy (TEM, JEOL JEM-2100), and X-ray photoelectron spectroscopy (XPS, PHI 5000 VersaProbe).

The UV−vis spectrum of the diffuse reflectance was measured from a Shimadzu UV-2600 recording spectrophotometer, from which the band gap energy was determined using the Tauc plot method. Photoluminescence(PL)spectroscopy was employed to study the recombination of electron and hole layers.

Electrochemical attributes were then examined potentiostically using the chronoamperometry method. All electrochemical measurements were conducted using Ag/AgCl as the reference electrode in the usual three-electrode system.

2.4 PFC Setup

The PFC configuration was set up using a home-made single chamber reactor containing the g-C_3N_4/Cu_2O or $BiVO_4$/Cu_2O as photocathode and a WO_3/TiO_2 as photoanode (Bachri *et al*., 2025). The electrolyte was a 0.3 M KOH solution containing crude palm oil mill effluent (POME) adjusted to a chemical oxygen demand (COD) concentration of 100 mgL^{-1}. System illumination was provided by a 3 W LED light source with a 410–420 nm wavelength to mimic the visible light condition. Gas chromatography (GC, Shimadzu GC-2014 fitted) was used to determine hydrogen production quantitatively. The electric current produced by the system was recorded by a digital multimeter in an external circuit.

3. Results and Discussion

3.1 Structural and Morphological Characterization

Figure 1 shows XRD patterns that reveal the crystal structure and phase purity of the produced photocathodes. According to the JCPDS card No. 05-0667 (Lv *et al*., 2018), the g-C_3N_4/Cu_2O photocathode exhibited diffraction peaks that were similar to the (111), (200), and (220) facets of the cubic-phase Cu_2O at the 2 tetha value (36.4°, 42.3°, and 61.3°). The (002) plane reflection of g-C_3N_4 which arises from the interlayer stacking of aromatic structures in the polymeric graphitic structure, was evidenced by a broad diffraction peak at roughly

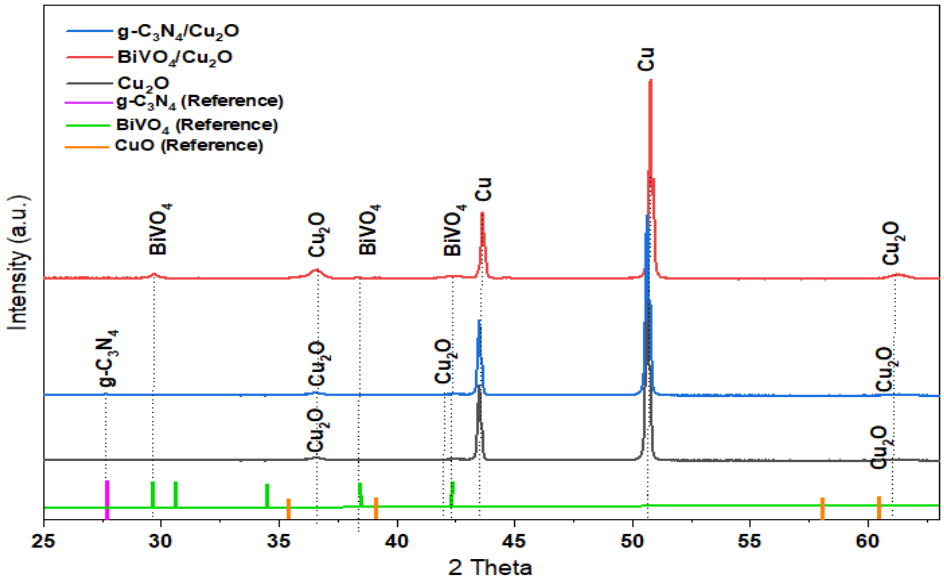

Fig. 1 Simulated XRD patterns of Cu_2O, $Cu_2O/g\text{-}C_3N_4$, and $Cu_2O/BiVO_4$ photocathodes (Source of g-C3N4: (Niaz *et al.*, 2023); BiVO4: (Cai *et al.*, 2023); CuO: (Uma *et al.*, 2021))

27.4°. The fact that the Cu_2O and $g\text{-}C_3N_4$ diffraction peaks were present together indicated that the p–n heterojunction structure also incorporated both components. (Zhang *et al.*, 2017; Cheng *et al.*, 2025).

The $BiVO_4/Cu_2O$ photocathode exhibited distinct peaks of Cu_2O, alongside additional peaks at 2θ = 28.8° and 47.2°, corresponding to the (121) and (040) planes of monoclinic scheelite-type $BiVO_4$ (JCPDS No. 14-0688 (Lin *et al.*, 2014). The results demonstrate the development of a well-crystallized $BiVO_4$ layer on the Cu_2O surface by the immersion-calcination method. No impurity phases were searched in both samples, indicating the good phase purity and crystallinity of the two heterojunction photocathodes. The successful construction of $g\text{-}C_3N_4/Cu_2O$ and $BiVO_4/Cu_2O$ heterostructures indeed offered a good basis for improved charge separation and the visible-light-driven photocatalytic performance, which was further validated by the investigations on the morphology, optical, and electrochemical properties in the following parts (Min *et al.*, 2014; (Hamdani & Bhaskarwar, 2021).

The crystallite sizes of the different phases in the $g\text{-}C_3N_4/Cu_2O$ and $BiVO_4/Cu_2O$ photocathodes were estimated from the XRD patterns using the Scherrer equation (Table **1**). For both composites, the Cu_2O (111) reflection appeared at 2θ ≈ 36.5°, with FWHM values of 0.40° for $g\text{-}C_3N_4/Cu_2O$ and 0.37° for $BiVO_4/Cu_2O$, corresponded to crystallite sizes of 20.9 nm and 20.4 nm, respectively. This indicated that the modification of Cu_2O with $g\text{-}C_3N_4$ or $BiVO_4$ did not significantly alter the Cu_2O crystallite size, and that nanosized Cu_2O domains (≈21 nm) were preserved in both photocathodes.

In the $g\text{-}C_3N_4/Cu_2O$ sample, the (002) peak of $g\text{-}C_3N_4$ located at 2θ = 27.44° exhibited a relatively narrow FWHM of 0.11°, giving a crystallite size of 74.3 nm.

The larger crystallite size of $g\text{-}C_3N_4$ compared to Cu_2O suggested that $g\text{-}C_3N_4$ forms extended stacked domains that can act as a continuous light-absorbing and electron-transport layer in contact with the Cu_2O surface. In contrast, the monoclinic $BiVO_4$ phase in $BiVO_4/Cu_2O$, represented by the diffraction peak at 2θ = 28.80°, showed a broader FWHM of 0.26° and a smaller crystallite size of 29.6 nm. The presence of $BiVO_4$ nanocrystallites in this size range implied a high interface density between $BiVO_4$ and Cu_2O, which is beneficial for constructing an efficient heterojunction.

These results demonstrated that both composites consist of nanoscale Cu_2O domains (~21 nm) intimately coupled with either larger $g\text{-}C_3N_4$ crystallites (~74 nm) or $BiVO_4$ nanocrystallites (~30 nm). Such size combinations are expected to provide a good balance between crystallinity (which favors charge transport) and interfacial area (which favors charge separation), thereby supporting the enhanced photoelectrochemical and photocatalytic performance of the $g\text{-}C_3N_4/Cu_2O$ and $BiVO_4/Cu_2O$ photocathodes discussed in the following sections.

Table 1
XRD peak parameters and Scherrer crystallite sizes of Cu_2O, $g\text{-}C_3N_4$ and $BiVO_4$ phases in the composite photocathodes.

Sample	Phase	Peak (hkl)	2θ (°)	θ (°)	θ Rad	FWHM (°)	β (rad)	D (nm)
$g\text{-}C_3N_4/Cu_2O$	Cu_2O	-111	36.490	18.245	0.318	0.4	0.007	20.904
	$g\text{-}C_3N_4$	-002	27.440	13.720	0.239	0.11	0.002	74.312
$BiVO_4/Cu_2O$	Cu_2O	-111	36.480	18.240	0.318	0.37	0.006	20.384
	$BiVO_4$	-121	28.800	14.400	0.251	0.26	0.005	29.583

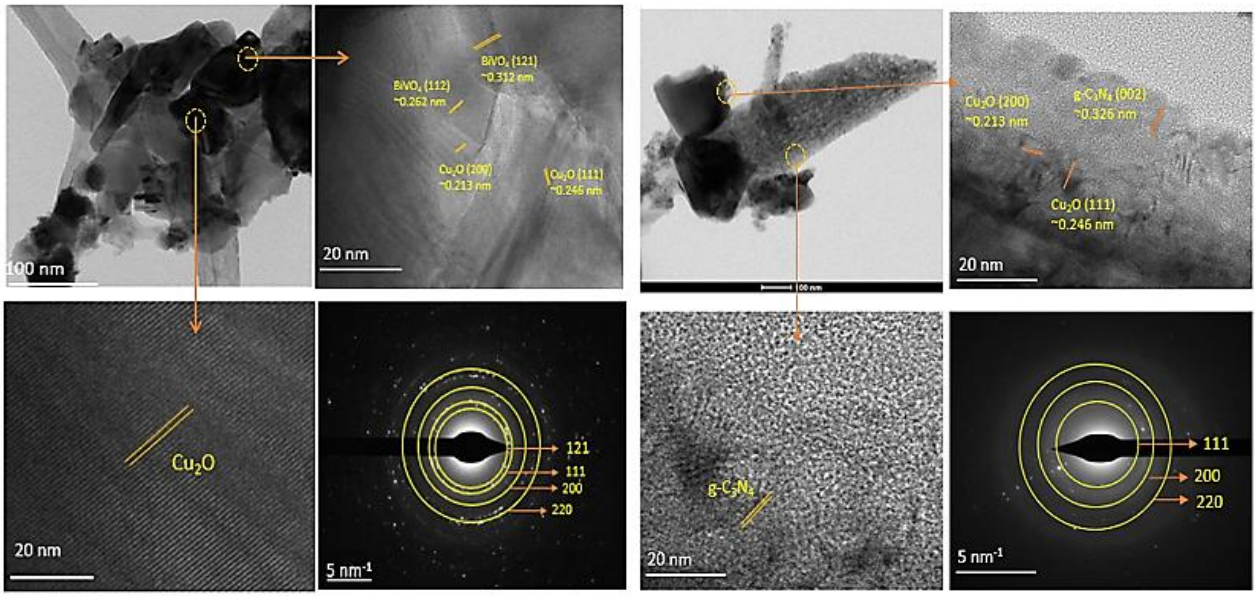

Fig. 2 The corresponding high-resolution TEM images, SAED patterns, and lattice fringes of (a). g-C_3N_4/Cu_2O (b). $BiVO_4$/Cu_2O photocathodes

3.2 Surface Morphology Analysis

The surface morphology and crystallographic structure of the photocathodes were investigated by HRTEM (high-resolution transmission electron microscopy), SAED (selected area electron diffraction), and lattice fringe imaging as well (Figure 2). The overlaid g-C_3N_4/Cu_2O and $BiVO_4$/Cu_2O layers were mainly well-shaped nanocubes, evenly adhering to the copper substrate (Kumar *et al*., 2016). The nanocubes exhibited sharp edges and clear lattice fringes corresponding to the (111) and (200) planes of Cu_2O, indicating a highly oriented structure produced by anodization.

The as-obtained g-C_3N_4/Cu_2O composite (Figure 2), in which the Cu_2O nanocubes of about 40–90 nm in size were uniformly loaded onto the surface of g-C_3N_4 nanowires (Yang *et al*., 2021), could be considered as a supporter framework. The bright and dark concave polygonal micro-structure of the g-C_3N_4 and Cu_2O phases suggested intimate interfacial contact at the boundary between them and demonstrated a good contrast difference between the two different components. Upon close examination, Cu_2O was still crystalline, whereas g-C_3N_4 seemed to be semi-amorphous, corresponding to the nature of its polymeric layer-like structure. Clear lattice fringes with an interplanar spacing of 0.246 nm were observed in the HRTEM picture (Figure 2), was in accordance with the (111) plane of the cubic Cu_2O (JCPDS 05-0667).

But g-C_3N_4 did not exhibit obvious fringes, indicating that it was semi-amorphous. Figure 2 also displayed an SAED pattern that indexed to a polycrystalline structure, with concentric diffraction rings that are indexed to the (111), (200), and (220) planes of Cu_2O. Figure 2 showed well-defined rings in the SAED pattern that correspond to the (111), (200), and (220) Cu_2O planes. It is expected that the Cu_2O nanocubes and the g-C_3N_4 nanowires are in strong contact, increasing the interfacial area between them. This increased interfacial area is expected to facilitate charge transfer and suppress electron–hole recombination.

On the contrary, there was a different interfacial configuration in the $BiVO_4$/Cu_2O photocathode. $BiVO_4$ nanoparticles were preferentially attached at the junctions between Cu_2O nanocubes (interparticle-bridging network, not full conformal coating) (A. Wang *et al*., 2015). This architecture provided the effective contact points between neighboring Cu_2O domains, and is expected to promote the directionality of the charge transport and the surface passivation. The HRTEM analysis showed lattice fringes from $BiVO_4$ with d spacings corresponding to (121) and (040) planes, while SAED patterns demonstrated a set of polycrystalline rings, suggesting well-crystalline $BiVO_4$ features in close proximity with Cu_2O.

3.3 Optical Properties and Band Gap Analysis

As shown in Figure 3, the photocathodes made of Cu_2O, g-C_3N_4/Cu_2O, and $BiVO_4$/Cu_2O have UV-Vis diffuse reflectance spectra (DRS). The absorption edge of the bare Cu_2O film was clearly approximately 620 nm, or 2.48 eV, in agreement with the characteristic of p-type Cu_2O semiconductors on the market. (Y. Zhang *et al*., 2023). The graphitic carbon nitride π-conjugated structure and band gap of 2.7 eV are responsible for the increased absorption intensity in the 430-450 nm region seen in the g-C_3N_4/Cu_2O photocathode after doping with g-C_3N_4. (Alhaddad *et al*., 2020).

The inclusion of g-C_3N_4 enhances absorption in the higher photon energy range with limited response to the long-wavelength visible light, as shown by the somewhat lower band gap of 2.51 eV, as demonstrated by the Tauc plot analysis. According to Cheng *et al*. (2025), $BiVO_4$ had a band gap of around 2.4 eV, whereas the $BiVO_4$/Cu_2O photocathode showed a second absorption edge at 490 nm. In comparison to bulk Cu_2O and g-C_3N_4/Cu_2O, the effective band gap calculated using the Tauc plot technique was 2.2 eV, suggesting that coupling with $BiVO_4$ may increase photon utilization under solar irradiation by expanding the absorption range into the longer visible light. (G. Li *et al*., 2025). Using the Kubelka-Munk function, the optical band gap energy was determined using Tauc plots (J. Zhang *et al*., 2024). According to the calculations, the bandgap energies of g-C_3N_4 /Cu_2O, Cu_2O, and $BiVO_4$ are 2.51 eV, 2.48 eV, and 2.2 eV, respectively.

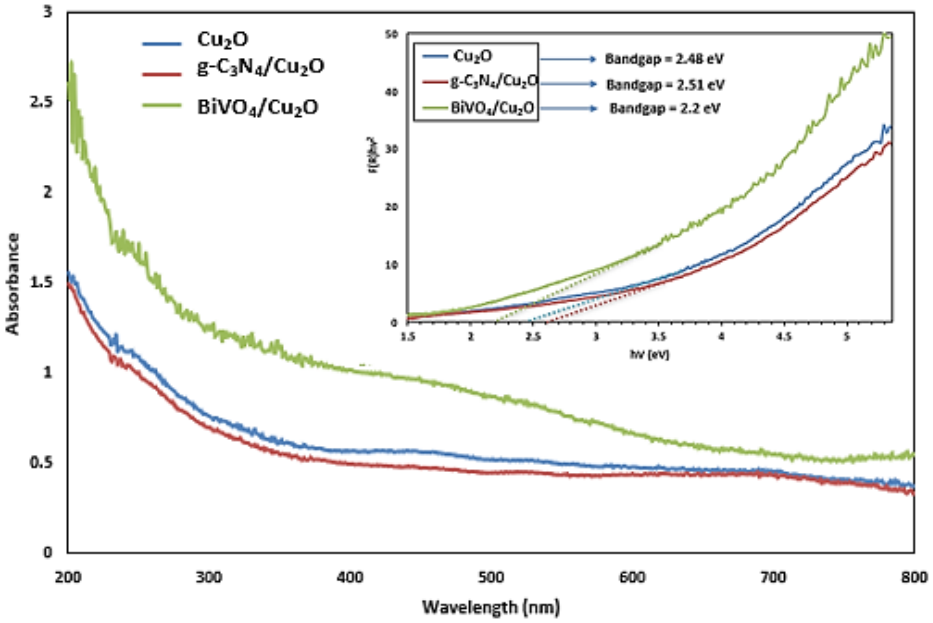

Fig. 3 UV–vis diffuse reflectance spectra (DRS) and Tauc plot analysis of Cu_2O, g-C_3N_4/Cu_2O, and $BiVO_4$/Cu_2O photocathodes

In both systems, the band edge alignments of the heterojunctions are expected to enhance the charge separation generated by visible light. The internal electric field is used to separate photogenerated carriers in the g-C_3N_4/Cu_2O system, which is achieved by creating a p-n heterojunction. (Anandan *et al*., 2017). On the other hand, a type-II or Z-scheme structure may work better at the $BiVO_4$/Cu_2O interface, allowing for efficient electron-hole transmission across the interface while minimizing recombination loss. (Cheng *et al*., 2025). To improve the working performance in solar-driven hydrogen evolution and wastewater degradation in PFCs, the optical characteristics show that the two heterojunction photocathodes could absorb a broad spectrum of visible light.

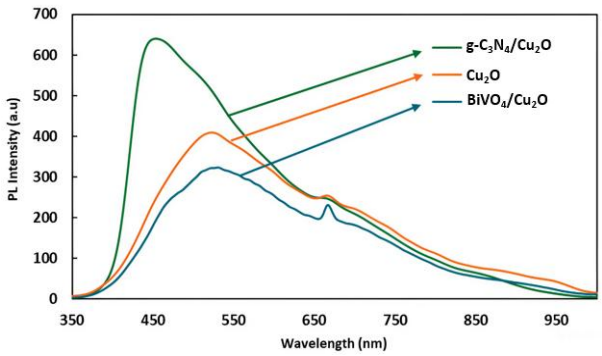

Fig. 4 Steady-state photoluminescence (PL) spectra of Cu_2O, g-C_3N_4/Cu_2O, and $BiVO_4$/Cu_2O photocathod

3.4 Photoluminescence (PL) Analysis

In order to learn about the photocathode materials' photogenerated electron-hole pair recombination, steady-state PL spectroscopy was used. Under illumination at 325 nm, the photoluminescence (PL) emission spectra of the clean Cu_2O, g-C_3N_4/Cu_2O, and $BiVO_4$/Cu_2O are shown in Fig. 4. Figure 4 shows the photoluminescence (PL) spectra of the photocathodes. At around 630 a.u., the g-C_3N_4/Cu_2O composite exhibited the highest PL intensity of all the samples. The efficient recombination of photo-excited electron-hole pairs indicated by such high radiative recombination, which suggests that the interfacial contact between Cu_2O and g-C_3N_4 is not ideal for splitting charges.

The medium amount of carrier recombination was indicated by the weak PL emission with a peak intensity of around 420 a.u. from the as-prepared Cu_2O electrode. Despite being lower than g-C_3N_4/Cu_2O, it indicated a limited carrier lifetime and poor charge-separation efficiency. Alternatively, the $BiVO_4$/Cu_2O photocathode did not exhibit this property, and out of all the samples, its PL band had the least intensity at about 325 a.u. The photo-generated carriers in the sample indicated a much lower recombination rate and the most efficient charge separation is shown by the evident PL quenching. A type-II or Z-schemed heterojunction is essential for effective charge transfer across interfaces and for extending carrier lifetimes; the quenching of PL is a reaction to the advantageous band configuration between $BiVO_4$ and Cu_2O at the interface.

Furthermore, the FWHM values of the heterostructured samples were seen to be narrower in comparison to Cu_2O, indicating a little improvement in the spectra. This finding suggests that the charge transport energy level becomes more evenly distributed when the defect-related recombination center decreases (Min *et al*., 2014). Collectively, the photoluminescence (PL) findings show that the $BiVO_4$/Cu_2O heterojunction engineering dramatically improves photoelectrochemical performance and significantly reduces recombination losses.

3.5 X-ray Photoelectron Spectroscopy (XPS)

The surface composition and chemical states of the g-C_3N_4/Cu_2O and $BiVO_4$/Cu_2O photocathodes were thoroughly investigated using X-ray photoelectron spectroscopy (XPS). The g-C_3N_4/Cu_2O system's Cu 2p spectrum showed two main peaks

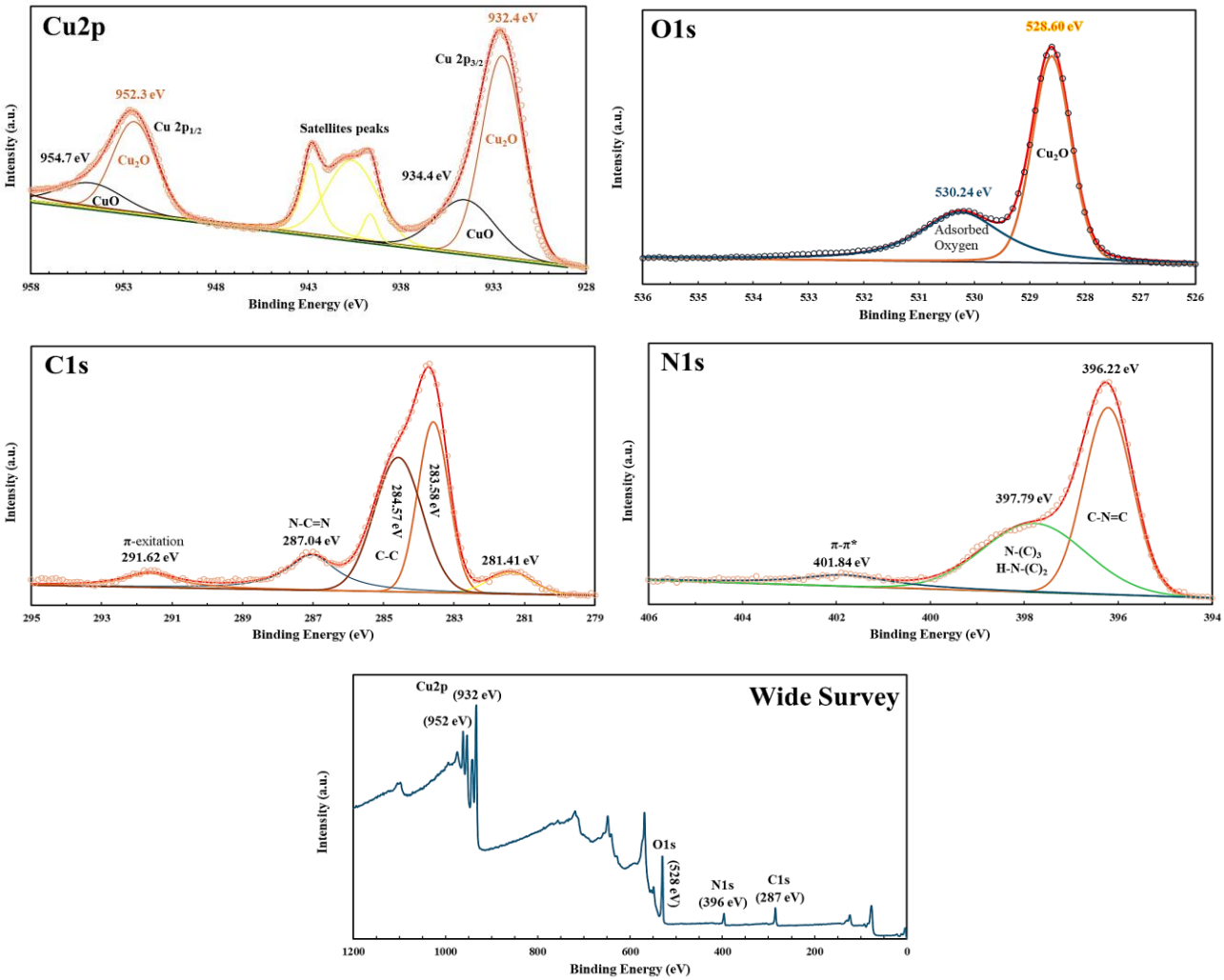

Fig. 5(a) XPS survey spectrum of g-C_3N_4/Cu_2O photocathode.

at 932.4 eV (Cu 2p 3/2) and 952.3 eV (Cu 2p 1/2), which was associated with Cu(I) species of Cu_2O. There were also shake-up satellite features between 941 and 945 eV, and a wider shoulder between 933 and 934.5 eV, which were indicative of the presence of some Cu(II) species, which are similar to CuO. The values observed in copper oxides are in agreement with the spin-orbit splitting of about 19.9 eV for Cu $2p_{1/2}$ and Cu $2p_{3/2}$. Based on these findings, it seems that the photocathode is mostly an oxidation state of Cu(I) species in Cu_2O, with the presence of Cu(II) resulting from surface partial oxidation. Despite its $2p_{3/2}$ peak at 932 eV and lack of satellite characteristics, metallic Cu (Cu^0) was not as noticeable as a significant component. Therefore, Cu_2O was the main component of the photocathode, whereas surface oxidation contributed to the remaining CuO.

There were two separated peaks in the O 1s peak, one at 528.60 eV and the other at 530.24 eV. The energy at 529.2 = 0.2 eV for Cu_2O, which is the lower binding energy (BE), was associated with lattice oxygen in the CuO phase (G. Li *et al.*, 2025), while the higher BE is thought to be caused by surface adsorbed oxygen or oxygen vacancies, the latter of which are active sites in photo-catalytic materials due to charge separation. According to Zeng *et al.* (2024), the photo-catalytic activity might be enhanced by using the adsorbed oxygen as electron traps.

In the C 1s spectrum, three peaks were resolved. The C-C bond, often caused by adventitious carbon or structural defect, was responsible for the main peak at 284.57 eV. The N=C-N bond coming from g-C_3N_4 (heptazine units) is corresponding to the second peak at about 287.04 eV. The aromatic system's π-π* shake-up transitions give rise to an additional satellite peak at 291.62 eV, suggesting a greater connection between the π-electron clouds in g-C_3N_4 as compared to ordinary C_3N_4. At 396.22 eV, 397.79 eV, and 401.84 eV, there were three components to the N 1s spectra. The C-N = C bonds, which are characteristic of heptazine rings in g-C_3N_4, are thought to be responsible for the main peak at 396.22 eV (Y. Liu *et al.*, 2019). It is possible to attribute the second signal at 397.79 eV, which indicates bonding with three carbon atoms, to nitrogen in an N-$(C)_t$ or H-N-$(C)_2$ environment. The aromatic polymer chains' π-π* satellite nitrogen transitions were responsible for the high-binding energy peak seen at 401.84 eV.

The expected behavior for copper oxides was seen in the copper 2p region XPS spectra of the $BiVO_4$/Cu_2O photocathode. At 932.4 eV, the primary peak emerged from Cu (I) species in Cu_2O; at 933–934 eV, a much weaker shoulder emerged; and at 936–940 eV, shake-up satellite peaks emerged, which are ascribed to a small percentage of Cu(II) species (CuO-like). The findings showed that the Cu $2p_{1/2}$ peak was similar with the results for copper oxide (Ahmed *et al.*, 2020), with a

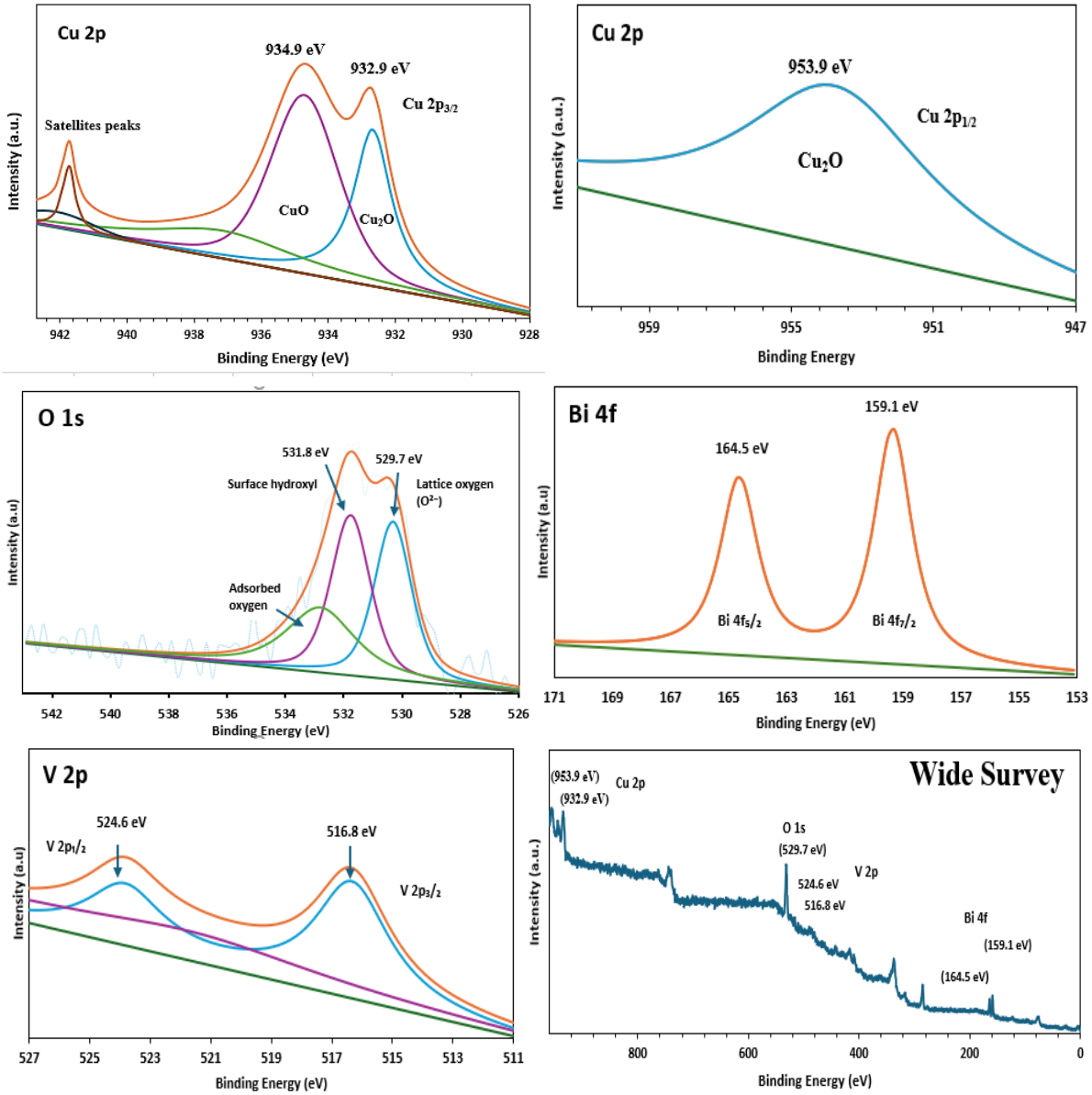

Fig. 5(b) XPS survey spectrum of $BiVO_4/Cu_2O$ photocathode

spin-orbit splitting of p 19.9 eV and a center at around 952.3 eV. Surprisingly, in the Cu $2p_1/_2$ area (955-962 eV), which is consistent with the intensity level of Cu(I) species, no extra satellite feature was seen. It has been confirmed by these results that Cu_2O is the most abundant copper species in the photocathode, with CuO exhibiting only a little amount, as is the case with most Cu-based photocatalysts. For photoelectrochemical activity and effective charge separation, a high Cu(I) concentration is ideal, whereas interfacial reactions might benefit from additional surface states offered by Cu(II).

Consistent with $BiVO_4$, the well-defined peaks of the Bi 4f region at 158.6 eV (Bi $4f_7/_2$) and 164.0 eV (Bi $4f_5/_2$) suggest the existence of the stable oxide Bi^{3+}. The absence of a reduction to V^{4+}, as shown by the peaks at 516.8 eV (V $2p_{3/2}$) and 524.2 eV (V $2p_{1/2}$) in V 2p, bodes poorly for the photocatalytic activities. Both the crystal lattice oxygen in VO_4 and Cu_2O and the surface hydroxyl groups or adsorbed oxygen on the bismuth vanadate surface were identified in the O 1s spectra of $BiVO_4/Cu_2O$, with the former peaking at 529.8 eV and the latter at 531.5 eV, respectively (Y. Zhang *et al.*, 2023). The photocatalytic activity is enhanced by photogenerated electron trapping, and these oxygen-absorbed species are crucial for triggered interfacial redox processes. The heterojunction has the potential to improve the photocatalytic and photoelectrochemical capabilities, since each component has retained its physicochemical characteristics while the Cu_2O loaded with g-C_3N_4 and $BiVO_4$ worked well together.

High-resolution XPS (Table 2) confirms the coexistence of Cu^+ and Cu^{2+} species in both $BiVO_4/Cu_2O$ and g-C_3N_4/Cu_2O photocathodes. In $BiVO_4/Cu_2O$, Cu^+ in Cu_2O accounts for roughly 70% of the Cu 2p envelope, while surface Cu^{2+} (CuO-like) contributes the remaining ~30%, indicating that Cu_2O is still the dominant copper phase with only partial surface oxidation. The O 1s region is composed of lattice O^{2-}, surface hydroxyls, and adsorbed oxygen in comparable proportions, and the Bi 4f and V 2p spectra show single Bi^{3+} and V^{5+} doublets, confirming the presence of stoichiometric $BiVO_4$ in the composite. For g-C_3N_4/Cu_2O, the relative fractions of Cu^+ (~72%) and Cu^{2+} (~28%) are similar, again suggesting a Cu_2O-rich bulk covered by a thin oxidized layer. The O 1s spectrum is

Table 2
Deconvolution of high-resolution XPS spectra for Cu, O, Bi, V, C and N species on $BiVO_4/Cu_2O$ and g-C_3N_4/Cu_2O photocathodes.

Sample	Element	Core level	Main Assignment	Area	Area (%)
$BiVO_4/Cu_2O$	Cu	Cu $2p_{3/2}$	Cu^+ in Cu_2O	955.55	18.52
			Cu^{2+} in CuO (surface)	1548.83	30.02
		Cu $2p1/_2$	Cu^+ in Cu_2O	2654.25	51.45
	O	O 1s	Lattice Oxygen	711.69	34.38
			Surface Hydroxyl	763.14	36.86
			Adsorbed Oxygen	595.30	28.76
	Bi	Bi 4f	Bi^{3+} in $BiVO_4$	1317.69	100.00
	V	V 2p	V^{5+} in $BiVO_4$	645.72	100.00
g-C_3N_4//Cu_2O	Cu	Cu $2p_{3/2}$	Cu^+ in Cu_2O	313000.90	48.85
			Cu^{2+} in CuO (surface)	118919.40	18.56
		Cu $2p1/_2$	Cu^+ in Cu_2O	149142.80	23.28
			Cu^{2+} in CuO (surface)	59680.66	9.31
	O	O 1s	Lattice Oxygen	104196.00	59.92
			Adsorbed Oxygen	69700.54	40.08
	C	C 1s	π–π*	3128.98	7.42
			N–C=N	7304.66	17.33
			C–C / C=C	17691.80	41.97
			C–M / carbide-like C (C–metal)	14555.10	34.53
			carbide-like/strongly reduced C	2597.74	6.16
	N	N 1s	C-N=C	14892.09	51.35
			N-$C_{(3)}$, H-N-$C_{(2)}$	11537.14	39.78
			phi-phi*	2572.42	8.87

dominated by lattice oxygen and adsorbed oxygen species, while the C 1s region reveals contributions from C–C/C=C, N–C=N in the g-C_3N_4 framework, and a significant share of C–M (carbide-like) species, evidencing strong interfacial bonding between g-C_3N_4 and Cu_2O. The N 1s spectrum, characterized by C–N=C and higher-binding-energy N–$(C)_3$/H–N–C components together with a weak π–π* feature, further corroborates the formation of conjugated g-C_3N_4 domains. These surface chemical states support the existence of intimate heterojunctions that are favourable for charge separation in both composite photocathodes.

3.6 Photoelectrochemical Performance

The photoelectrochemical characteristics of the Cu_2O photoelectrodes were also studied in terms of amperometric I–t measurements under chopped visible-light illumination with a bias of –0.5 V vs Ag/AgCl (Figure 6). The as-synthesized Cu_2O electrode showed – 0.025 mA/cm² steady-state photocurrent current density with the lowest photocurrent response among all samples, due to poor charge separation and fast electron–hole recombination. The g-C_3N_4/Cu_2O photocathode presented a slight increase up to -0.035 mA/cm² of stable photocurrent density, indicating that a p-n junction between Cu_2O and g-C_3N_4 was constructed, which could effectively facilitate charge carrier separation and transfer in comparison with CN-absent Cu_2O (Bae *et al*., 2024).

In contrast, peak photocurrent density was achieved for $BiVO_4/Cu_2O$ at around – 0.10 mA/cm² during light ON cycles

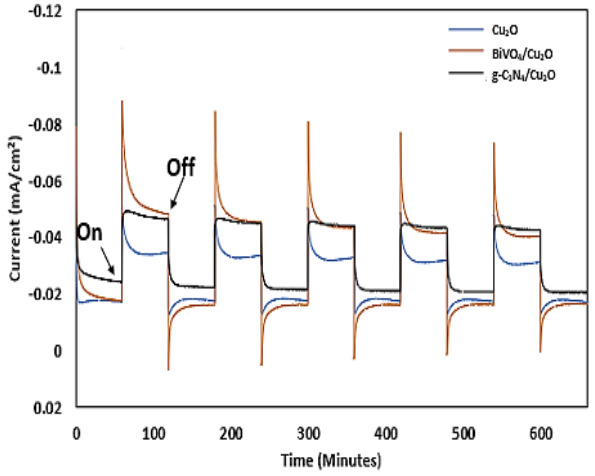

Fig. 6 Amperometric I–t curves of g-C_3N_4/Cu_2O and $BiVO_4/Cu_2O$ photocathodes at a bias of –0.5 V vs Ag/AgCl

and finally evolved to ~ –0.04 mA/cm². This remarkable enhancement could be ascribed to the good band edge matching and efficient interfacial charge transfer, which result in the inhibition of recombination losses between $BiVO_4$ and Cu_2O (Shu *et al.*, 2025).

The repeated ON–OFF cycles confirmed the stable and reproducible photoresponse of all photocathodes, with $BiVO_4/Cu_2O$ showing the strongest and most durable performance. These results clearly establish that incorporating $BiVO_4$ into Cu_2O was more effective in enhancing photocathodic activity than g-C_3N_4 modification.

3.7 Photocatode Stability

The stability trends shown in Figure 6 clearly distinguished the durability of the three photocathodes through their photocurrent behavior during repeated light on/off cycles. $BiVO_4/Cu_2O$ consistently produced the highest photocurrent peaks, and the amplitude of these peaks remained largely preserved throughout the sequence, indicating minimal performance decay and highly efficient charge extraction under illumination. The slight downward drift observed after several cycles is modest compared to the other samples, demonstrating that $BiVO_4$ effectively mitigates the photocorrosion typically experienced by Cu_2O. Even after approximately four hours of operation, only faint localized darkening appeared on the surface, confirming that the structural integrity of the photocathode remains largely intact. In comparison, pristine Cu_2O showed moderate but relatively steady photocurrent responses, suggesting acceptable short-term stability but limited catalytic capability due to weak intrinsic charge separation. On the other hand, g-C_3N_4/Cu_2O exhibited the lowest photocurrent and the most pronounced cycle-to-cycle degradation, reflected by progressively diminishing peak intensities and visible surface deterioration such as darkening and roughened regions.

3.8 Analysis of Performance Testing for the PFC System

The stable and repeatable photoresponse for all photocathodes was verified using repeated ON–OFF cycles, where a $BiVO_4/Cu_2O$ exhibited the highest and most durable performance. The results unambiguously demonstrate that $BiVO_4$ modification is much more effective in promoting the photocathodic activity than concurrent functionalization of g-C_3N_4.

3.8.1 Electricity Generation Performance

The current and power density characteristics, as shown in Figures 7(a) and 7(b), provide an electricity generation analysis. The electrical performance of the PFC cells indicateed that the $BiVO_4/Cu_2O$ photocathode bearing system was the most efficient compared to pristine Cu_2O, and the g-C_3N_4/Cu_2O photocathode showed the lowest reported performance. It was found that after 240 minutes of continuous photoelectrochemical operation, current and power densities of $BiVO_4/Cu_2O$ reached around 0.0098 mA cm^{-2} and 0.05625 mW cm^{-2}, respectively, which were higher than those of pristine Cu_2O (0.0076 mA cm^{-2}; 0.0375 mW cm^{-2}) and g-C_3N_4/Cu_2O (0.0052 mA cm^{-2}; 0.0260 mW cm^{-2}).

The $BiVO_4/Cu_2O$ photoelectrode exhibited a significant enhancement in photocurrent and power generation, attributable to the interparticle bridging architecture of $BiVO_4/Cu_2O$, where $BiVO_4$ nanoparticles preferentially develop along Cu_2O nanocubes, forming conductive junctions that

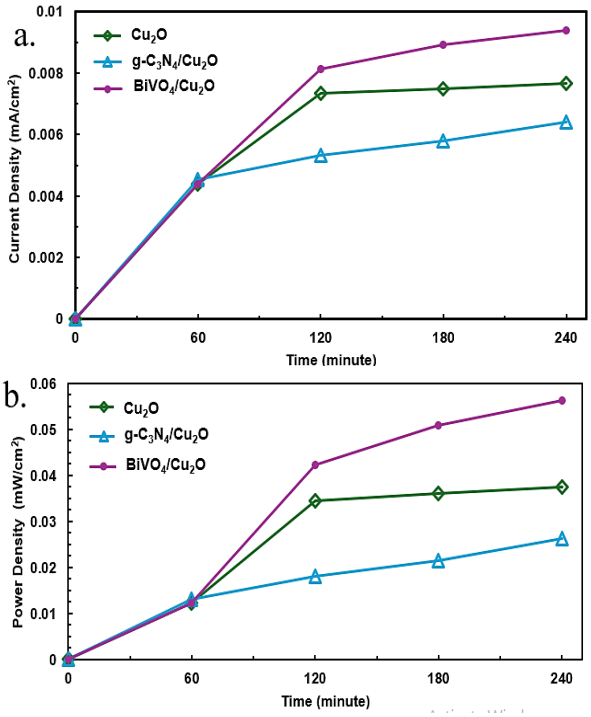

Fig 7. (a) Current Density of Cu_2O, g-C_3N_4/Cu_2O and BiVO4/Cu_2O photocathode 7(b) Power Density of Cu_2O, g-C_3N_4/Cu_2O and BiVO4/Cu_2O photocathode

facilitate efficient directional charge transfer while minimizing electron–hole recombination. $BiVO_4$ may be illuminated by visible light, resulting in the transport of photogenerated electrons from the conduction band of $BiVO_4$ to the conduction band of Cu_2O, establishing advantageous energy levels (N. Li *et al.*, 2024). This synergistic electron transfer enhanced the electron availability for the hydrogen evolution process (HER), improved external circuit flow, and increases both HER efficiency and total power output. (Zhou *et al.*, 2025).

However, the electrical output of the g-C_3N_4/Cu_2O photocathode was lower than that of $BiVO_4/Cu_2O$ and pristine Cu_2O, which can be ascribed to suboptimal interfacial matching and low mobility in the operating state within the nanowire n etwork. These results also agree with previous reports on the critical importance of heterojunction engineering and interfacial optimization for photocurrent density and power output in PFC systems (Kee *et al.*, 2020; Slamet *et al.*, 2022; Pratiwi *et al.*, 2023).

3.8.2 Hydrogen Production Analysis

Figure 8 illustrates that the system based on the PFC with $BiVO_4/Cu_2O$ photocathode produced the largest amount of hydrogen of 13.71 mmol m^{-2} for cumulative volume, even for the longer time (240 min), which is slightly higher than that for the pure Cu_2O (11.19 mmol m^{-2}) or Cu_2O/g-C_3N_4 (8.16 mmol m^{-2}). The excellent HER performance of $BiVO_4/Cu_2O$ can be ascribed to a unique interparticle bridging structure, since the $BiVO_4$ nanoparticles anchoring with Cu_2O nanocubes selectively to build conductive interparticle bridges further and approach the interface contact, promote directional charge transfer, and suppress the recombination of electron holes.

Under visible-light irradiation, $BiVO_4$ could absorb photons and quickly separate photoinduced electrons in its conduction band (CB), which were transferred to the CB of Cu_2O because of its well-engineered band structure. These electrons

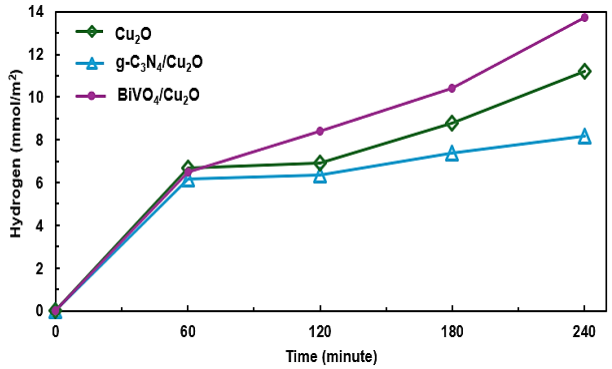

Fig. 8 Hydrogen evolution of Cu_2O, g-C_3N_4/Cu_2O and $BiVO_4$/Cu_2O photocathode.

then further catalyzed HER at the surface of the photocathode. On the other hand, photogenerated holes in $BiVO_4$ could be transferred to the electrolyte and trigger oxidation reactions. The excellent hydrogen production suggested that the interfacial structure of $BiVO_4$/Cu_2O suppressed the recombination in the photocatalyst and coordinates well the visible-light absorption, charge separation and surface reaction.

In contrast, g-C_3N_4/Cu_2O photocathode showed a relatively poorer hydrogen evolution activity, although the formation of a p–n junction between Cu_2O nanocubes and one-dimensional g-C_3N_4 nanowires was favorable for hydrogen evolution. The decreased hydrogen evolution was probably attributed to inefficient interfacial coupling and restricted charge mobility in the g-C_3N_4 network, thereby slowing down efficient electron transfer during operation.

These results agree with previous findings that rational heterojunction design and nanostructure engineering are two important strategies in order to enhance the hydrogen evolution performance in PFC systems (Husein *et al.*, 2024; Muttaqin *et al.*, 2022; Yu *et al.*, 2024).

3.8.3 Mechanism of Heterojunction in g-C_3N_4/Cu_2O and $BiVO_4$/Cu_2O Photocathodes

The heterojunction formed between Cu_2O and its combined materials (g-C_3N_4 or $BiVO_4$) is instrumental in critically influences the overall performance of the PFC system (such as charge separation, electricity generation, and hydrogen generation). According to the experimental result, it was believed that the g-C_3N_4/Cu_2O photocathode is dominated by the Type-II p–n heterojunction process (Chen *et al.*, 2014), and the $BiVO_4$/Cu_2O photocathode has a more Z-scheme path (Khan *et al.*, 2022). They play a vital role in charge separation efficiency, recombination of electron-hole, and the redox potentials of active species (Ge *et al.*, 2019; Z. Wang *et al.*, 2021). To further substantiate these proposed charge-transfer pathways, electrochemical impedance spectroscopy (EIS) (Figure 9) was employed to probe the interfacial kinetics at the photocathode/electrolyte interface.

Electrochemical impedance spectroscopy (EIS) was carried out to gain further insight into the interfacial charge-transfer properties of the different photocathodes. The Nyquist plots in Fig. 9 exhibited a single depressed semicircle for all samples, characteristic of a charge-transfer process at the electrode/electrolyte interface that can be described by a simple Randles-type circuit. The diameter of the semicircle is directly related to the charge-transfer resistance (Rct): a smaller semicircle reflects a lower Rct and thus a faster interfacial charge-transfer rate. Fitting of the spectra yielded Rct values of ≈8.0 kΩ for g-C_3N_4/Cu_2O, ≈3.0 kΩ for bare Cu_2O, and only ≈0.5 kΩ for $BiVO_4$/Cu_2O, while the solution resistances R_1 remained relatively small (≈50, 90, and 30 Ω, respectively).

A clear trend was observed in which $BiVO_4$/Cu_2O shows the smallest semicircle and the lowest Rct, followed by bare Cu_2O, whereas g-C_3N_4/Cu_2O displays the largest semicircle and the highest Rct. This ordering (Rct,$BiVO_4$/Cu_2O < Rct,Cu_2O < Rct,g-C_3N_4/Cu_2O) was fully consistent with the photoelectrochemical and photocatalytic performances, where $BiVO_4$/Cu_2O outperforms Cu_2O and g-C_3N_4/Cu_2O. The pronounced decrease in Rct upon coupling Cu_2O with $BiVO_4$ indicated that the $BiVO_4$/Cu_2O junction provided an additional, energetically favourable pathway for charge transport and effectively suppressed interfacial recombination. In contrast, the larger semicircle and high Rct of g-C_3N_4/Cu_2O suggested a less efficient charge-transfer process, likely due to higher resistance across the g-C_3N_4 layer and/or less favourable band alignment. Taken together with the band-structure discussion, these EIS results strongly supported the formation of an efficient heterojunction in $BiVO_4$/Cu_2O, which facilitated directional charge separation and underpins its superior overall performance. When exposed to visible light, the Cu_2O/$BiVO_4$ Z-scheme heterojunction created photoinduced electrons (e^-) and holes (h^+). At the interparticle bridging contact, the valence

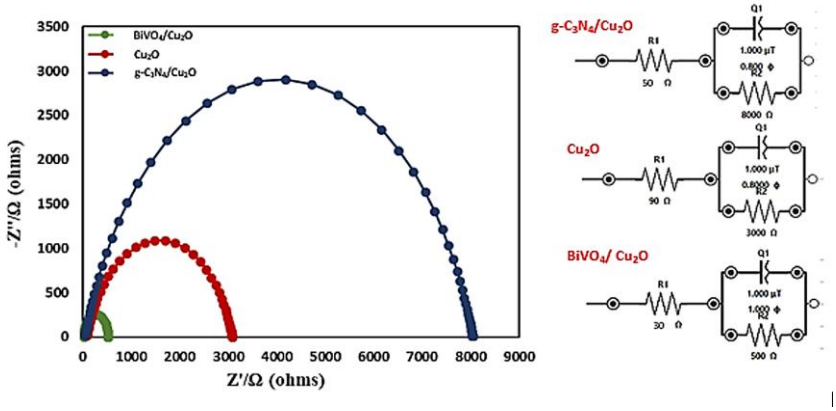

Fig 9. Nyquist plots and corresponding equivalent circuit models for Cu_2O, g-C_3N_4/Cu_2O and $BiVO_4$/Cu_2O photocathodes.

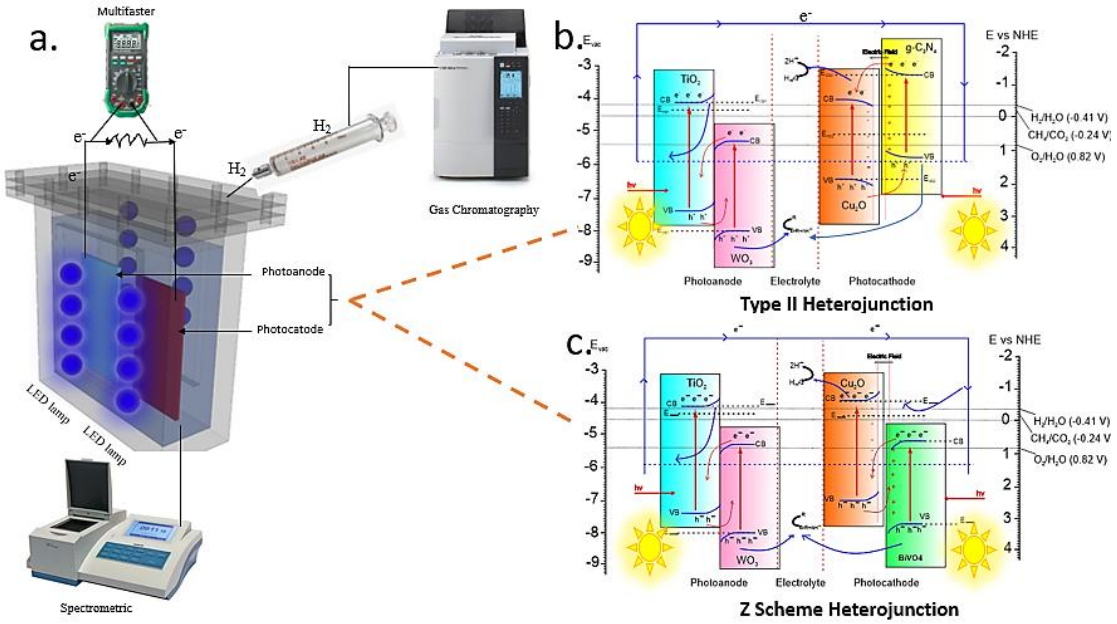

Fig. 10 (a) Predicted Schematic design of the photocatalysis-fuel cell reactor system with a WO_3/TiO_2-NT/Ti photoanode and g-C_3N_4/Cu_2O and $BiVO_4/Cu_2O$ photocathode. (b) Prediction illustration of the charge transfer mechanism via a type-II heterojunction, and (c) Prediction via a Z-scheme heterojunction.

band holes of Cu_2O recombined with the conduction band electrons of $BiVO_4$. At the conduction band of Cu_2O, the reaction created electrons that were highly reducing, whereas at the valence band of $BiVO_4$, the reaction created holes that were very oxidizing. Concequently $BiVO_4/Cu_2O$ performed very well in the simultaneous generation of electricity and hydrogen due to its better redox potentials, excellent interfacial charge transfer mechanism, and reduced bulk recombination.

The Type-II g-C_3N_4/Cu_2O heterojunction showed a staggered band alignment that moved electrons from g-C_3N_4 conduction band (CB) to Cu_2O CB (-1.1 V vs NHE) and holes from Cu_2O's valence band (VB) to g-C_3N_4 VB (+0.7 V vs NHE). The electron-hole recombination was effectively prevented by this spatial separation, although the redox potential was lower than in the Z-scheme system. As a result, when contrasted with $BiVO_4/Cu_2O$, the g-C_3N_4/Cu_2O photocathode produced less hydrogen and had lower electrical output.

The interface structure in both systems, together with the expected direction of charge migration and Fermi levels, is shown schematically in Figure 10. The emphasis is on the distinctions between the Type-II (g-C_3N_4/Cu_2O) and Z-scheme ($Cu_2O/BiVO_4$) processes. By selectively recombining low-energy carriers, the Z-scheme $Cu_2O/BiVO_4$ heterojunction might improve the exploitation of redox activity for PFC applications. On the other hand, the redox capacity is diminished in the Type-II g-C_3N_4/Cu_2O heterojunction, which primarily encourages spatial separation of the charges.

4. Conclusion

It is worth noting the different behaviors of Cu_2O-based photocathodes used in conjunction with g-C_3N_4 and $BiVO_4$ in the PFC electrodes. The $BiVO_4/Cu_2O$ hybrid exhibited superior activity, delivering the highest hydrogen evolution rate (13.71 mmol m^{-2}) and maximum power density (0.05625 mW cm^{-2}) at 240 minutes, attributed to a proton gradient-driven Z-scheme heterojunction with a type-II interparticle bridging structure that promoting efficient charge transfer and suppresses carrier recombination. Direct Cu_2O displayed moderate activity (11.19 mmol m^{-2}, 0.0375 mW cm^{-2}), whereas g-C_3N_4/Cu_2O showed the lowest activity (8.16 mmol m^{-2}, 0.0260 mW cm^{-2}), clearly reflecting unsatisfactory charge separation and low redox potentials. These results underscore that interface optimization and band alignment are critical, and position the $BiVO_4/Cu_2O$-based photocathode as one of the most promising candidates for PFC devices for hydrogen production and power generation. It should be noted, however, that the assignment of Type-II (g-C_3N_4/Cu_2O) and Z-scheme ($BiVO_4/Cu_2O$) mechanisms remains largely inferential from photoelectrochemical, XPS, and EIS data, and future studies employing advanced spectroscopies such as ESR, transient photovoltage/photocurrent, or transient absorption will be required to directly verify the charge-transfer pathways.

The novelty of this work is twofold. First, a flat Cu plate was directly converted into Cu_2O and subsequently modified into two distinct heterojunctions, affording stronger interfacial contact, shorter electron pathways, and a more facile fabrication route than conventional FTO, ITO, carbon cloth, or Cu foam substrates. Second, both heterojunctions were integrated into a single-chamber PFC that simultaneously generated hydrogen and electricity, enabling a direct comparison of Cu_2O-based heterostructures under identical conditions. These outcomes highlight the importance of interface engineering and firmly establish $BiVO_4/Cu_2O$ as a promising photocathode for future PFC applications.

Acknowledgments

Universitas Indonesia provided support for this work through a Seed Funding Professor grant. The first author's doctoral program in Chemical Engineering was made possible by the scholarship provided by Beasiswa Pendidikan Indonesia (BPI/The Indonesian Education Scholarship), the Center for Higher Education Funding and Assessment, the Ministry of Higher Education, Science, and Technology of the Republic of Indonesia, and the Endowment Fund for Education Agency (LPDP), Ministry of Finance of the Republic of Indonesia. The authors are grateful for their support. The authors also express

their gratitude to the Department of Chemical Engineering at FTUI for the research facilities and the National Research and Innovation Agency of Indonesia (BRIN), Forensic Laboratory Center of Criminal Investigation Agency, Indonesian National Police (PUSLABFOR POLRI), and Integrated Laboratory and Research Center, Universitas Indonesia (ILRC UI), for the photocathode characterization.

Author Contributions M.F.H.**:** Principal investigator responsible for data collection and primary data analysis. M.F.B.: Led the research, made methods and initial data processing. R.: Contributed to manuscript writing and helped with methodology, material collection, and purchase. R.Y.: Carried out materials characterization and participated in data interpretation. M.I.: Analysis and processing of photoelectrochemical properties data S.: Conceived the original idea and research plans, guided methodology, reviewed and revised the manuscript. All authors have read and agreed to the final version of the manuscript.

Funding: This research was supported by a Seed Funding Professor grant from Universitas Indonesia. The authors also express appreciation to BPI, the Center for Higher Education Funding and Assessment, and LPDP for the scholarship support provided.

Conflicts of Interest: The authors have no conflicts of interest in publishing this paper. Funder All funders and sponsors had no role in this research's design, conduct or interpretation.

References

Ahmed, A. M., Abdalla, E. M., & Shaban, M. (2020). Simple and Low-Cost Synthesis of Ba-Doped CuO Thin Films for Highly Efficient Solar Generation of Hydrogen. *Journal of Physical Chemistry C*, *124*(41), 22347–22356. https://doi.org/10.1021/acs.jpcc.0c04760

Alhaddad, M., Navarro, R. M., Hussein, M. A., & Mohamed, R. M. (2020). Visible light production of hydrogen from glycerol over Cu2O-gC3N4 nanocomposites with enhanced photocatalytic efficiency. *Journal of Materials Research and Technology*, *9*(6), 15335–15345. https://doi.org/10.1016/j.jmrt.2020.10.093

Anandan, S., Wu, J. J., Bahnemann, D., Emeline, A., & Ashokkumar, M. (2017). Crumpled Cu2O-g-C3N4 nanosheets for hydrogen evolution catalysis. *Colloids and Surfaces A: Physicochemical and Engineering Aspects*, *527*(May),34–41. https://doi.org/10.1016/j.colsurfa.2017.05.007

Bachri, M. F., Husein, S., & Heru, B. (2025). *Development of WO 3 / TiO 2 -NT / Ti photoanode for simultaneously POME degradation , electricity generation , and hydrogen production in a photocatalysis-fuel cell system*. *15*(3), 420–428. https://doi.org/10.61435/ijred.2025.6097

Bae, H., Bhamu, K. C., Mane, P., Burungale, V., Kumar, N., Lee, S. H., Ryu, S. W., Kang, S. G., & Ha, J. S. (2024). Rationally designed core-shell of 2D-g-C3N4/Cu2O nanowires heterojunction photocathode for efficient photoelectrochemical water splitting. *Materials Today Energy*, *40*, 101484. https://doi.org/10.1016/j.mtener.2023.101484

Chen, J., Shen, S., Guo, P., Wang, M., Wu, P., Wang, X., & Guo, L. (2014). In-situ reduction synthesis of nano-sized Cu2O particles modifying g-C3N4 for enhanced photocatalytic hydrogen production. *Applied Catalysis B: Environmental*, *152–153*(1), 335–341. https://doi.org/10.1016/j.apcatb.2014.01.047

Cheng, Y., Yu, T., Lei, X., Li, J., You, J., Liu, X., & Guo, R. (2025). Construction of charge transport channels and strong interfacial electric fields in BiVO4/Cu2O Type-II heterojunction for enhanced piezo-photocatalytic performance. *Journal of Environmental Chemical Engineering*, *13*(3), 116763. https://doi.org/10.1016/j.jece.2025.116763

Dai, B., Li, Y., Xu, J., Sun, C., Li, S., & Zhao, W. (2022). Photocatalytic oxidation of tetracycline, reduction of hexavalent chromium and hydrogen evolution by Cu2O/g-C_3N_4 S-scheme photocatalyst: Performance and mechanism insight. *Applied Surface Science*, *592*(March), 153309. https://doi.org/10.1016/j.apsusc.2022.153309

Ge, J., Zhang, Y., Heo, Y. J., & Park, S. J. (2019). Advanced design and synthesis of composite photocatalysts for the remediation of wastewater: A review. In *Catalysts* (Vol. 9, Issue 2). https://doi.org/10.3390/catal9020122

Hamdani, I. R., & Bhaskarwar, A. N. (2021). Cu2O nanowires based p-n homojunction photocathode for improved current density and hydrogen generation through solar-water splitting. *International Journal of Hydrogen Energy*, *46*(55), 28064–28077. https://doi.org/10.1016/j.ijhydene.2021.06.067

Hayat, A., Sohail, M., El Jery, A., Al-Zaydi, K. M., Alshammari, K. F., Khan, J., Ali, H., Ajmal, Z., Taha, T. A., Ud Din, I., Altamimi, R., Hussein, M. A., Al-Hadeethi, Y., Orooji, Y., & Ansari, M. Z. (2023). Different Dimensionalities, Morphological Advancements and Engineering of g-C3N4-Based Nanomaterials for Energy Conversion and Storage. *Chemical Record*, *23*(5). https://doi.org/10.1002/tcr.202200171

He, Y., Zhang, C., Hu, J., & Leung, M. K. H. (2019). NiFe-layered double hydroxide decorated BiVO4 photoanode based bi-functional solar-light driven dual-photoelectrode photocatalytic fuel cell. *Applied Energy*, *255*, 113770. https://doi.org/https://doi.org/10.1016/j.apenergy.2019.113770

Husein, S., Slamet, & Dewi, E. L. (2024). A review on graphite carbon nitride (g-C3N4)-based composite for antibiotics and dye degradation and hydrogen production. *Waste Disposal & Sustainable Energy*, *6*(4), 603–635. https://doi.org/10.1007/s42768-024-00198-y

Kee, M. W., Lam, S. M., Sin, J. C., Zeng, H., & Mohamed, A. R. (2020). Explicating charge transfer dynamics in anodic TiO2/ZnO/Zn photocatalytic fuel cell for ameliorated palm oil mill effluent treatment and synchronized energy generation. *Journal of Photochemistry and Photobiology A: Chemistry*, *391*(September 2019), 112353. https://doi.org/10.1016/j.jphotochem.2019.112353

Khan, N., Stelo, F., Santos, G. H. C., Rossi, L. M., Gonçalves, R. V., & Wender, H. (2022). Recent advances on Z-scheme engineered BiVO4-based semiconductor photocatalysts for CO2 reduction: A review. *Applied Surface Science Advances*, *11*(March), 100289. https://doi.org/10.1016/j.apsadv.2022.100289

Kumar, S., Parlett, C. M. A., Isaacs, M. A., Jowett, D. V., Douthwaite, R. E., Cockett, M. C. R., & Lee, A. F. (2016). Facile synthesis of hierarchical Cu2O nanocubes as visible light photocatalysts. *Applied Catalysis B: Environmental*, *189*, 226–232. https://doi.org/10.1016/j.apcatb.2016.02.038

Li, G., Jin, Y., Li, Y., Cui, W., An, H., Li, R., & Li, C. (2025). Cu/Cu2O nanoparticles supported on electrospun carbon nanofibers as high-performance cathodic catalyst for photocatalytic fuel cell. *Journal of Colloid and Interface Science*, *699*(P2), 138270. https://doi.org/10.1016/j.jcis.2025.138270

Li, N., Mao, S., Yan, W., & Zhang, J. (2024). Photo-induced in-situ synthesis of Cu2O@C nanocomposite for efficient photocatalytic evolution of hydrogen. *Ranliao Huaxue Xuebao/Journal of Fuel Chemistry and Technology*, *52*(5), 698–706. https://doi.org/10.1016/S1872-5813(23)60400-1

Li, R., Chen, H., Xiong, J., Xu, X., Cheng, J., Liu, X., & Liu, G. (2020). A mini review on bismuth-based z-scheme photocatalysts. *Materials*, *13*(22), 1–29. https://doi.org/10.3390/ma13225057

Lin, X., Yu, L., Yan, L., Li, H., Yan, Y., Liu, C., & Zhai, H. (2014). Visible light photocatalytic activity of BiVO4 particles with different morphologies. *Solid State Sciences*, *32*, 61–66. https://doi.org/10.1016/j.solidstatesciences.2014.03.018

Liu, W., Liu, X., Xin, S., Wang, Y., Huo, S., Fu, W., Zhao, Q., Gao, M., & Xie, H. (2024). Photocatalytic fuel cell assisted by Fenton-like reaction for p-Chloronitrobenzen degradation and electricity production through S-scheme heterojunction C3N5 modified TNAs photoanode: Performance, DFT calculation and mechanism. *Applied Energy*, *358*. https://doi.org/10.1016/j.apenergy.2023.122552

Lu, B. B., Lu, J. C., Zhao, Q. Y., Wang, R., Chen, Z. L., Guan, J. Q., Liu, H., Fu, Y., & Ye, F. (2025). Enhanced electron transport through

hydrogen bonds and Ag nanoparticles in the PCN-222/Ag/COF core–shell photocatalyst for efficient oxytetracycline degradation. *Journal of Cleaner Production*, *494*(February), 144995. https://doi.org/10.1016/j.jclepro.2025.144995

Lv, Y., Shi, B., Su, X., & Tian, L. (2018). Synthesis and characterization of Cu2O nanowires array via an anodic oxidation method. *Materials Letters*, *212*, 122–125. https://doi.org/10.1016/j.matlet.2017.09.120

Mamari, S. Al, Kuvarega, A. T., & Selvaraj, R. (2021). Recent advancements in the development of graphitic like carbon nitride (G-C3N4) photocatalyst for volatile organic compounds removal: A review. *Desalination and Water Treatment*, *235*, 141–176. https://doi.org/10.5004/dwt.2021.27633

Min, S., Wang, F., Jin, Z., & Xu, J. (2014). Cu2O nanoparticles decorated BiVO4 as an effective visible-light-driven p-n heterojunction photocatalyst for methylene blue degradation. *Superlattices and Microstructures*, *74*, 294–307. https://doi.org/10.1016/j.spmi.2014.07.003

Muttaqin, R., Pratiwi, R., Ratnawati, Dewi, E. L., Ibadurrohman, M., & Slamet. (2022). Degradation of methylene blue-ciprofloxacin and hydrogen production simultaneously using combination of electrocoagulation and photocatalytic process with Fe-TiNTAs. *International Journal of Hydrogen Energy*, *47*(42), 18272–18284. https://doi.org/10.1016/j.ijhydene.2022.04.031

Ni, N., Li, H., He, L., Zhou, J., Sang, Z., Liu, Y., du, S., Wang, Q., & Tong, Y. (2022). Structures and photocatalytic activities of bismuth oxyhalides nanoparticles developed by utilizing a simple reaction. *Materials Science and Engineering: B*, *286*(September), 116031. https://doi.org/10.1016/j.mseb.2022.116031

Pratiwi, R., Ibadurrohman, M., Dewi, E. L., & Slamet. (2023). A novel approach in the synthesis of CdS/titania nanotubes array nanocomposites to obtain better photocatalyst performance. *Communications in Science and Technology*, *8*(1), 16–24. https://doi.org/10.21924/cst.8.1.2023.1049

Rehan, M. A., Li, G., Liang, H., & Ali, M. (2025). Recent advances in hybrid photocatalysts for efficient solar photocatalytic hydrogen production. *International Journal of Hydrogen Energy*, *97*(August 2024), 920–949. https://doi.org/10.1016/j.ijhydene.2024.11.420

Shu, X., Wang, R., Yang, L., Liu, S., Yin, Y., Liang, X., Hu, K., & Zhang, M. (2025). Bifunctional BiVO4/Cu2O photoelectrode for bias-free solar water splitting tandem cells. *Solar Energy Materials and Solar Cells*, *282*(December 2024), 113386. https://doi.org/10.1016/j.solmat.2024.113386

Sienkiewicz, A., Wanag, A., Kusiak-Nejman, E., Ekiert, E., Rokicka-Konieczna, P., & Morawski, A. W. (2021). Effect of calcination on the photocatalytic activity and stability of TiO2photocatalysts modified with APTES. *Journal of Environmental Chemical Engineering*, *9*(1), 104794. https://doi.org/10.1016/j.jece.2020.104794

Slamet, S., Pelawi, L. F., Ibadurrohman, M., Yudianti, R., & Ratnawati. (2022). Simultaneous Decolorization of Tartrazine and Production of H2 in a Combined Electrocoagulation and Photocatalytic Processes using CuO-TiO2 Nanotube Arrays: Literature Review and Experiment. *Indonesian Journal of Science and Technology*, *7*(3), 385–404. https://doi.org/10.17509/ijost.v7i3.51315

Uma, B., Anantharaju, K. S., Renuka, L., Nagabhushana, H., Malini, S., More, S. S., Vidya, Y. S., & Meena, S. (2021). Controlled synthesis of (CuO-Cu2O)Cu/ZnO multi oxide nanocomposites by facile combustion route: A potential photocatalytic, antimicrobial and anticancer activity. *Ceramics International*, *47*(10), 14829–14844. https://doi.org/10.1016/j.ceramint.2020.09.223

Wang, A., Shen, S., Zhao, Y., & Wu, W. (2015). Preparation and characterizations of BiVO4/reduced graphene oxide nanocomposites with higher visible light reduction activities. *Journal of Colloid and Interface Science*, *445*, 330–336. https://doi.org/10.1016/j.jcis.2015.01.017

Wang, Z., Lin, Z., Shen, S., Zhong, W., & Cao, S. (2021). Advances in designing heterojunction photocatalytic materials. *Chinese Journal of Catalysis*, *42*(5), 710–730. https://doi.org/10.1016/S1872-2067(20)63698-1

Yang, B., Wang, Z., Zhao, J., Sun, X., Wang, R., Liao, G., & Jia, X. (2021). 1D/2D carbon-doped nanowire/ultra-thin nanosheet g-C3N4 isotype heterojunction for effective and durable photocatalytic H2 evolution. *International Journal of Hydrogen Energy*, *46*(50), 25436–25447. https://doi.org/10.1016/j.ijhydene.2021.05.066

Yu, H., Wang, Y., & Wang, X. (2024). Synthesis of a Z-scheme photocatalyst (P-doped g-C3N4/Bi3+-doped Ag3PO4) and its photocatalytic performance. *Journal of Industrial and Engineering Chemistry*, *130*, 436–445. https://doi.org/10.1016/j.jiec.2023.09.049

Zeng, C., Tsui, L. S., Lam, F. L. Y., Wu, T., & Yip, A. C. K. (2024). Revisiting the crucial roles of oxygen vacancies in photo/electro-catalytic degradation of aqueous organic pollutants. *Applied Catalysis O: Open*, *190*(March), 206930. https://doi.org/10.1016/j.apcato.2024.206930

Zhang, J., Shi, T., Liu, T., Gao, F., Cai, D., Liu, P., Yang, S., & zhang, Y. (2024). Design and synthesis of a UV–vis-NIR response heterostructure system: For efficient solar energy conversion and BPA photocatalytic degradation. *Applied Surface Science*, *653*(December 2023), 159346. https://doi.org/10.1016/j.apsusc.2024.159346

Zhang, P., Wang, T., & Zeng, H. (2017). Design of Cu-Cu 2 O/g-C 3 N 4 nanocomponent photocatalysts for hydrogen evolution under visible light irradiation using water-soluble Erythrosin B dye sensitization. *Applied Surface Science*, *391*, 404–414. https://doi.org/10.1016/j.apsusc.2016.05.162

Zhang, Y., Zhang, Z., Zhang, Y., Li, Y., & Yuan, Y. (2023). Shape-dependent synthesis and photocatalytic degradation by Cu2O nanocrystals: Kinetics and photocatalytic mechanism. *Journal of Colloid and Interface Science*, *651*(July), 117–127. https://doi.org/10.1016/j.jcis.2023.07.196

Zhou, J., Tian, Y., Gu, H., & Jiang, B. (2025). Photocatalytic hydrogen evolution: Recent advances in materials, modifications, and photothermal synergy. *International Journal of Hydrogen Energy*, *115*(March), 113–130. https://doi.org/10.1016/j.ijhydene.2025.03.088